Mon. Not. R. Astron. Soc. **000**, 000–000 (0000) Printed 17 September 2014 (MN LATEX style file v2.2)

ASASSN-14ae: A Tidal Disruption Event at 200 Mpc

T. W.-S. Holoien[1], J. L. Prieto[2,3,4], D. Bersier[5], C. S. Kochanek[1,6], K. Z. Stanek[1,6], B. J. Shappee[1], D. Grupe[7,8], U. Basu[1,9], J. F. Beacom[1,6,10], J. Brimacombe[11], J. S. Brown[1], A. B. Davis[10], J. Jencson[1], G. Pojmanski[12] and D. M. Szczygieł[12]

[1] *Department of Astronomy, The Ohio State University, 140 West 18th Avenue, Columbus, OH 43210, USA*
[2] *Department of Astrophysical Sciences, Princeton University, 4 Ivy Lane, Peyton Hall, Princeton, NJ 08544, USA*
[3] *Núcleo de Astronomía de la Facultad de Ingeniería, Universidad Diego Portales, Av. Ejército 441, Santiago, Chile*
[4] *Millennium Institute of Astrophysics*
[5] *Astrophysics Research Institute, Liverpool John Moores University, 146 Brownlow Hill, Liverpool L3 5RF, UK*
[6] *Center for Cosmology and AstroParticle Physics (CCAPP), The Ohio State University, 191 W. Woodruff Ave., Columbus, OH 43210, USA*
[7] *Swift MOC, 2582 Gateway Dr., State College, PA 16802, USA*
[8] *Space Science Center, Morehead State University, 235 Martindale Dr., Morehead, KY 40351, USA*
[9] *Grove City High School, 4665 Hoover Road, Grove City, OH 43123, USA*
[10] *Department of Physics, The Ohio State University, 191 W. Woodruff Ave., Columbus, OH 43210, USA*
[11] *Coral Towers Observatory, Cairns, Queensland 4870, Australia*
[12] *Warsaw University Astronomical Observatory, Al. Ujazdowskie 4, 00-478 Warsaw, Poland*

17 September 2014

ABSTRACT

ASASSN-14ae is a candidate tidal disruption event (TDE) found at the center of SDSS J110840.11+340552.2 ($d \simeq 200$ Mpc) by the All-Sky Automated Survey for Supernovae (ASAS-SN). We present ground-based and *Swift* follow-up photometric and spectroscopic observations of the source, finding that the transient had a peak luminosity of $L \simeq 8 \times 10^{43}$ erg s^{-1} and a total integrated energy of $E \simeq 1.7 \times 10^{50}$ ergs radiated over the ~ 5 months of observations presented. The blackbody temperature of the transient remains roughly constant at $T \sim 20,000$ K while the luminosity declines by nearly 1.5 orders of magnitude during this time, a drop that is most consistent with an exponential, $L \propto e^{-t/t_0}$ with $t_0 \simeq 39$ days. The source has broad Balmer lines in emission at all epochs as well as a broad He II feature emerging in later epochs. We compare the color and spectral evolution to both supernovae and normal AGN to show that ASASSN-14ae does not resemble either type of object and conclude that a TDE is the most likely explanation for our observations. At $z = 0.0436$, ASASSN-14ae is the lowest-redshift TDE candidate discovered at optical/UV wavelengths to date, and we estimate that ASAS-SN may discover $0.1 - 3$ of these events every year in the future.

Key words: accretion, accretion disks — black hole physics — galaxies: nuclei

1 INTRODUCTION

When a star's orbit brings it within the tidal disruption radius of a supermassive black hole (SMBH), the tidal shear forces become more powerful than the star's self-gravity and the star breaks apart. Roughly half of the mass of the star is ejected while the rest of the stellar material remains bound to the black hole and is accreted. These tidal disruption events (TDEs) result in a short-lived ($t \lesssim 1$ yr) accretion flare (Lacy et al. 1982; Phinney 1989; Rees 1988; Evans & Kochanek 1989). For $M_{BH} \lesssim 10^7 M_\odot$, the initial fallback rate is super-Eddington and the eventual rate at which material returns to pericenter becomes a $t^{-5/3}$ power law (Evans & Kochanek 1989; Phinney 1989). While it is commonly assumed that the resulting luminosity is proportional to this rate of return to pericenter, this is only a crude approximation to the complex physics associated with evolution of the accretion stream (Kochanek 1994), and the exact return rates depend on, for example, the structure of the star (e.g., Lodato & Rossi 2011).

In the most luminous phases, TDE emission is likely dominated by a photosphere formed in the debris rather than any direct emission from a hot accretion disk (Evans & Kochanek 1989; Loeb & Ulmer 1997; Ulmer 1999; Strubbe & Quataert 2009). Only in the late phases, as the debris becomes optically thin, will there be any direct emission from the disk. The exact balance likely depends on the viewing angle, as illustrated by the simulations of Guillochon,

Manukian & Ramirez-Ruiz (2014). Observationally, TDEs would be expected to show spectral characteristics and light curve evolution that would distinguish them from both supernovae (SNe) and normal active galactic nuclei (AGN), and the detection and study of TDEs remains a useful avenue for studying the properties of SMBHs despite their low predicted frequency ($(1.5-2.0)^{+2.7}_{-1.3} \times 10^{-5}$ yr^{-1} per galaxy; van Velzen & Farrar 2014), as the light emitted during the TDE flare may be sensitive to the black hole spin and mass (e.g., Ulmer 1999; Graham et al. 2001).

At present candidate TDEs can be divided into two observational classes based on the wavelength at which they were discovered. The first consists of those found in UV and X-ray surveys, such as candidates in NGC5905 (Komossa & Bade 1999) and IC3599 (Grupe et al. 1995; Brandt, Pounds & Fink 1995), a candidate in the galaxy cluster A1795 (Donato et al. 2014), Swift J164449.3+573451 (Burrows et al. 2011; Bloom et al. 2011; Levan et al. 2011; Zauderer et al. 2011), Swift J0258.4+0516 (Cenko et al. 2012b), and GALEX candidates D1-9, D3-13, and D23H-1 (Gezari et al., 2008; Gezari et al. 2009). These typically do not have strong optical emission. The second consists of those found in optical surveys, including PTF10iya (Cenko et al. 2012a); SDSS TDE 1 and TDE 2 (van Velzen et al. 2011); PS1-10jh (Gezari et al. 2012); PS1-11af (Chornock et al. 2014); and PTF09ge, PTF09axc, PTF09djl, PTF10iam, PTF10nuj, and PTF11glr (Arcavi et al. 2014). While the X-ray candidates currently outnumber the optical and UV candidates, variable AGN activity can also mimic the behavior expected for TDEs in the X-ray, making it difficult to disentangle true TDEs from AGN (van Velzen et al. 2011). Modern wide-field optical transient surveys, such as the All-Sky Automated Survey for Supernovae (ASAS-SN[1]; Shappee et al. 2013), the Palomar Transient Factory (PTF; Law et al. 2009), and the Panoramic Survey Telescope & Rapid Response System (Pan-STARRS; Chambers 2007) allow for the identification and monitoring of such TDE candidate events on a rapid time cadence across many wavelengths, helping to differentiate true TDEs from AGN and SNe, and should prove a very useful resource for discovering TDFs in the future.

Here we describe the discovery and follow-up observations of ASASSN-14ae, a potential TDE. The transient was discovered by ASAS-SN, a long-term project to monitor the whole sky on a rapid cadence to find nearby supernovae and other bright transients (see Shappee et al. 2013 for details), such as AGN activity (e.g., Shappee et al. 2013), extreme stellar flares (e.g., Schmidt et al. 2014), outbursts in young stellar objects (e.g., Holoien et al. 2014), and cataclysmic variable stars (e.g., Stanek et al. 2013; Kato et al. 2013). Our transient source detection pipeline was triggered on 2014 January 25, detecting a new source with $V = 17.1 \pm 0.1$ mag (Prieto et al. 2014). The object was also detected on 2014 January 26 at roughly the same magnitude, but is not detected ($V \gtrsim 18$ mag) in data obtained on 2014 January 1 and earlier. A search at the object's position in the Sloan Digital Sky Survey Data Release 9 (SDSS DR9; Ahn et al. 2012) catalog revealed the source of the outburst to be the inclined spiral galaxy SDSS J110840.11+340552.2 at redshift $z = 0.0436$, corresponding to a luminosity distance of $d = 193$ Mpc ($H_0 = 70$ km s^{-1} Mpc^{-1}, $\Omega_M = 0.3$, $\Omega_\Lambda = 0.7$), and that the ASAS-SN source position was consistent with the center of the host galaxy. Follow-up images obtained on 2014 January 27 with the Las Cumbres Observatory Global Telescope Network (LCOGT) 1-m telescope at McDonald Observatory (Brown et al. 2013), the 2-m Liverpool Telescope (LT) (Steele et al. 2004), and the *Swift* UltraViolet and Optical Telescope (UVOT; Roming et al. 2005) confirmed the detection of the transient. After astrometrically aligning an LT image of the source in outburst with the archival SDSS image of the host galaxy, we measure an offset of 0.28 ± 0.45 pixels (0.09 ± 0.14 arcseconds) between the position of the brightest pixel in the host galaxy in the LT image and the position of the brightest pixel in the SDSS image. This indicates that the source of the new flux is consistent with the center of the galaxy, providing evidence for a TDE interpretation. Figure 1 shows the ASAS-SN V-band reference and subtracted images of the source as well as SDSS pre-discovery and LT g-band images.

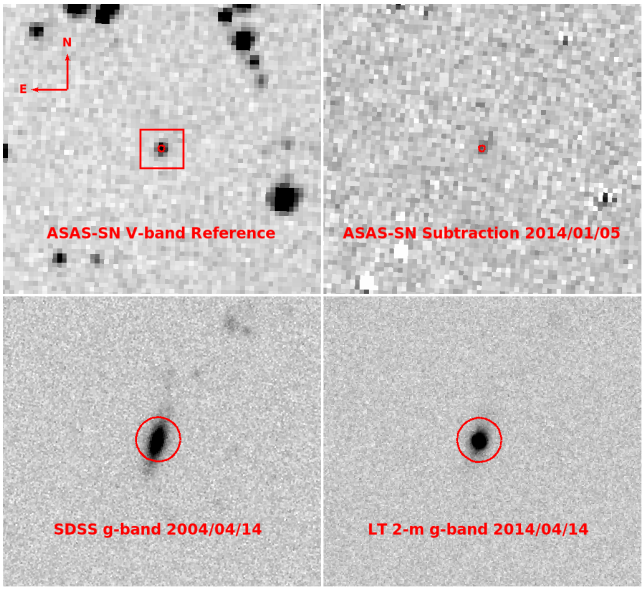

Figure 1. Discovery image of ASASSN-14ae. The top-left panel shows the ASAS-SN V-band reference image and the top-right panel shows the ASAS-SN subtracted image from 2014 January 25. The bottom-left panel shows the archival SDSS g-band image of the host galaxy and the bottom-right panel shows an LT 2-m g-band image from 2014 February 08. The dates of the observations are listed in each panel, and the lower panels show a smaller field of view, indicated by the red box in the top-left panel. The red circles have radii of 5.″0 and are centered on the host position.

The archival SDSS spectrum of the host is that of an early-type spiral with little evidence of emission lines from an AGN, although it does show [O III] 5007 in emission indicating that there is some recent star-formation. A transient classification spectrum obtained on 2014 January 29 with the Dual-Imaging Spectrograph (DIS) mounted on the Apache Point Observatory (APO) 3.5-m telescope showed a blue continuum as well as a broad (FWHM $\simeq$ 17000 km/s) Hα line. The blue continuum and Hα emission suggested that this transient was likely a young Type II SN, but the proximity to the galactic nucleus and its absolute magni-

[1] `http://www.astronomy.ohio-state.edu/~assassin/index.shtml`

Table 1. Photometry of Host Galaxy

Filter	Magnitude	Magnitude Uncertainty
u	19.16	0.03
g	17.60	0.02
r	16.94	0.02
i	16.65	0.02
z	16.45	0.02
J	15.34	0.05
H	14.73	0.10
K_s	14.34	0.10

These are 5.″0 radius aperture magnitudes from SDSS and 2MASS.

tude at discovery ($M_V \sim -19.3$ mag from the ASAS-SN host-subtracted image) made a tidal capture event a potential alternative. We decided to start a follow-up campaign in order to fully characterize this interesting transient.

In §2 we describe pre-outburst archival observations, including both photometry and spectroscopy of the host galaxy, as well as new data taken of the transient during our follow-up campaign. In §3 we analyze these data and describe the properties of the transient. Finally, in §4 we compare these properties to those of supernovae, AGN, and other proposed TDEs to examine the nature of the object.

2 OBSERVATIONS AND SURVEY DATA

In this section we summarize the available archival data of the transient host galaxy as well as our new photometric and spectroscopic observations of ASASSN-14ae.

2.1 Archival Photometry and Spectroscopy

We retrieved archival reduced images in *ugriz* of SDSS J110840.11+340552.2 from SDSS DR9. We then measured the fluxes in a 5.″0 aperture radius (the same aperture used to measure the source in follow-up data, chosen to match the *Swift* PSF and to minimize the effects of seeing variations on the photometry) to use for galaxy SED modeling and for subtracting the host galaxy fluxes from the transient fluxes. We also retrieved near-IR JHK_s images from the Two-Micron All Sky Survey (2MASS; Skrutskie et al. 2006) and measured aperture magnitudes of the host galaxy in the same fashion. The measured SDSS and 2MASS magnitudes of the host galaxy are presented in Table 1.

There are no archival Spitzer, Herschel, Hubble Space Telescope (HST), Chandra, or X-ray Multi-Mirror Mission (XMM-Newton) observations of the source. The host galaxy is not detected in the ROSAT All-Sky Survey with an upper flux limit of 3×10^{-13} erg s^{-1} cm^{-2} in the $0.1 - 2.4$ keV band (Voges et al. 1999), providing further evidence that the galaxy is inactive. We also retrieved archival mid-IR photometry from the Wide-field Infrared Survey Explorer (WISE; Wright et al. 2010). From the WISE $W1$ and $W2$ measurements we calculate that the host galaxy has $(W1 - W2) \simeq 0.06 \pm 0.06$ mag, and this blue mid-IR color is further evidence against AGN activity (e.g., Assef et al. 2013).

We used the code for Fitting and Assessment of Synthetic Templates (FAST v1.0; Kriek et al. 2009) to fit stellar population synthesis (SPS) models to the 5.″0 SDSS *ugriz* and 2MASS JHK_s magnitudes of the host galaxy. The fit was made assuming a CCM extinction law (Cardelli, Clayton & Mathis 1988) with $R_V = 3.1$, an exponentially declining star-formation history, a Salpeter IMF, and the Bruzual & Charlot (2003) models. We obtained a good SPS fit (reduced $\chi^2_\nu = 0.4$), with the following parameters: $A_V = 0.15^{+0.15}_{-0.15}$ mag, $M_* = (6.3^{+0.6}_{-0.8}) \times 10^9$ M$_\odot$, age$= 2.2^{+0.6}_{-0.2}$ Gyr, and SFR$= (3^{+5}_{-1}) \times 10^{-2}$ M$_\odot$ yr^{-1}. We note that these properties do not appear to be consistent with SDSS J110840.11+340552.2 being an E+A galaxy, as many of the hosts of the TDE candidates in Arcavi et al. (2014) were. The FAST estimate of $A_V = 0.15$ mag incorporates both Galactic and host extinction and this value is consistent with the Galactic extinction ($A_V = 0.057$ mag based on Schlafly & Finkbeiner 2011). In fits to the transient SED, we find no evidence for additional extinction, even though the *Swift* UV data, particularly the $UVM2$ band which lies on top of the 2200 Å extinction curve feature, is a powerful probe for additional dust (though this depends on the strength of the UV bump in the dust law). In the analyses of the event's SED which follow we only correct for this Galactic extinction.

We also obtained the spectrum of SDSS J110840.11+340552.2 from SDSS-DR9. The archival spectrum is dominated by absorption lines (e.g., Balmer lines, Ca I G-band, Mg I, Na I, Ca H&K, and the 4000 Å break) that are characteristic of intermediate-age and old stellar populations. This is consistent with the results of the FAST fit to the SED of the host. The spectrum does not show strong emission lines, except for the detection of an unresolved [O III] 5007 line with FWHM $\simeq$ 250 km s^{-1} and integrated luminosity L$_{[\rm O\,III]} \simeq 2.4 \times 10^{39}$ erg s^{-1}. This is likely a sign of a low level of recent star formation, indicating the galaxy could host core-collapse supernova events, but without detecting other emission lines (e.g., Hβ, Hα, [N II]) we cannot constrain the rate of star formation. We note that the [O III]/Hβ and [N II]/Hα ratios may indicate that the host contains a very weak Type 2 AGN, consistent with the analysis done in Arcavi et al. (2014). However, other factors (e.g., the WISE photometry) argue against significant activity.

We use the FWHM $\simeq$ 250 km s^{-1} of the [O III] line from the latest spectroscopic epoch, presented in §2.3, to estimate a velocity dispersion for the galaxy and place an upper limit on the mass of the black hole of $M_{BH} < 10^{6.8}$ M$_\odot$ using the M-σ relation from Gültekin et al. (2009). SDSS reports a velocity dispersion of $\sigma = 42.9 \pm 7.3$ km s^{-1}, which is well below the velocity resolution of the SDSS spectrograph of $\sim$ 100 km s^{-1}, so we will conservatively regard the SDSS estimate as a limit of $\sigma < 100$ km s^{-1}. Using the same M-σ relation from Gültekin et al. (2009) and the SDSS resolution of 100 km s^{-1} gives an upper limit of $M_{BH} \lesssim 10^{6.9}$ M$_\odot$, consistent with the limit we derive from the width of the [O III] line. Finally, from the FAST fit, we have $M_* \sim 10^{9.8}$ M$_\odot$, which is consistent with a bulge mass of $M_B \sim 10^{9.4}$ M$_\odot$ (Mendel et al. 2014). Using the M_B-M_{BH} relation from McConnell & Ma (2013) gives $M_{BH} \sim 10^{6.8}$ M$_\odot$, which is again consistent with the limits derived from the host and transient spectra.

2.2 New Photometric Observations

After detection of the transient, we were granted a series of *Swift* X-ray Telescope (XRT; Burrows et al. 2005) and UVOT target-of-opportunity (ToO) observations. The *Swift* UVOT observations of ASASSN-14ae were obtained in 6 filters: V (5468 Å), B (4392 Å), U (3465 Å), $UVW1$ (2600 Å), $UVM2$ (2246 Å), and $UVW2$ (1928 Å) (Poole et al. 2008). We used the UVOT software task *uvotsource* to extract the source counts from a 5.″0 radius region and a sky region with a radius of ∼40.″0. The UVOT count rates were converted into magnitudes and fluxes based on the most recent UVOT calibration (Poole et al. 2008; Breeveld et al. 2010). The UVOT Vega magnitudes are shown along with other photometric data in Figure 2.

The XRT was operating in Photon Counting mode (Hill et al. 2004) during our observations. The data from all epochs were reduced and combined with the software tasks *xrtpipeline* and *xselect* to obtain an image in the 0.3−10 keV range with a total exposure time of $\sim 42,030$ s. We used a region with a radius of 20 pixels (47.″1) centered on the source position to extract source counts and a source-free region with a radius of 100 pixels (235.″7) for background counts. We do not detect X-ray emission from ASASSN-14ae to a 3-sigma upper limit of 5.9×10^{-4} counts s^{-1}. To convert this to a flux, we assume a power law spectrum with $\Gamma = 2$ and Galactic H I column density (Kalberla et al. 2005), yielding an upper limit of $\sim 2.9 \times 10^{-14}$ erg cm^{-2} s^{-1}. At the host distance of $d = 193$ Mpc, this corresponds to an upper limit of $L_X \leq 1.3 \times 10^{41}$ erg s^{-1} (3.4×10^7 L$_\odot$) on the average X-ray luminosity. The constraints for the individual *Swift* epochs are on average ∼ 10 times weaker, and we only consider the combined X-ray limit.

In addition to the *Swift* observations, we obtained *gri* images with the LCOGT 1-m at the MacDonald Observatory and *ugriz* images with the LT 2-m telescope. We measured aperture photometry[2] using a 5.″0 aperture radius to match the host galaxy and *Swift* UVOT measurements. The photometric zero points were determined using several SDSS stars in the field. These data are shown in Figure 2.

Figure 2 shows the UV and optical light curves of ASASSN-14ae from MJD 56682.5 (the epoch of first detection) through our latest epoch of observations on MJD 56828 (146 days after first detection) without extinction correction or host flux subtraction. Also shown are the SDSS *ugriz* magnitudes and synthesized *Swift* UVOT magnitudes of the host galaxy extrapolated from the host SED fit. With the host flux included, the light curve shows ASASSN-14ae brightened much more strongly in the blue and UV filters than in the red bands, with the largest increase in the *Swift* $UVM2$ band (2246 Å), where it brightened by $\Delta m_{UVM2} \sim -4.9$. The brightness also appears to be declining at a faster rate with respect to the host in bluer filters. We further analyze this light curve and compare it to SNe and TDEs in the literature in §3.1.

After correcting our photometric measurements for Galactic extinction, we construct SEDs for 5 follow-up epochs. These are shown with the extinction-corrected SDSS archival data and host SED fit from FAST in Figure 3.

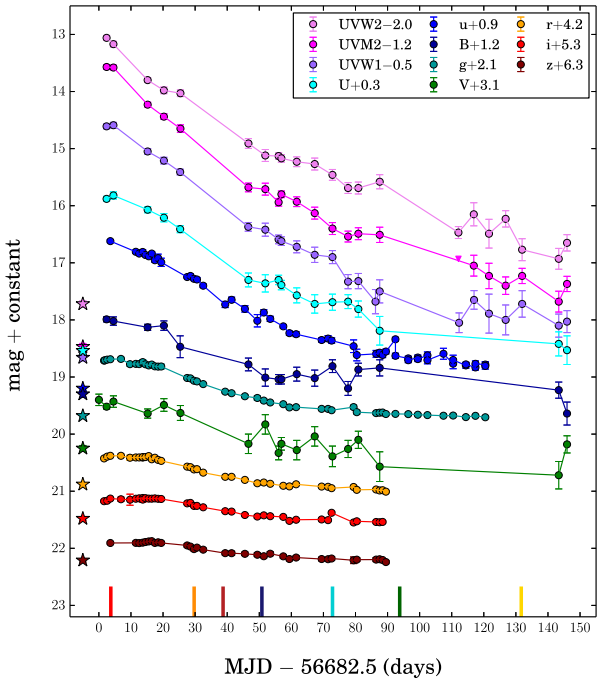

Figure 2. Light curves of ASASSN-14ae, starting at discovery (MJD = 56682.5) and spanning 146 days. Follow-up data obtained from *Swift* (UV + optical), the LCOGT 1-m (optical), and the LT 2-m (optical) are shown as circles. 3-sigma upper limits are shown as triangles for cases where the source is not detected. All magnitudes are shown in the Vega system. The data are not corrected for extinction and error bars are shown for all points, but in some cases they are smaller than the data points. Host galaxy magnitudes measured by SDSS in a 5.″0 aperture for *ugriz* and synthesized from our host SED model for the *Swift* UVOT bands are shown as stars at −5 days. Dates of spectroscopic follow-up are indicated with vertical bars at the bottom of the figure with colors matching the corresponding spectra in Figures 4 and 5. ASASSN-14ae brightened by nearly 5 magnitudes in the UV with respect to the host galaxy while brightening by a progressively smaller amount in redder filters. The relative decline rate with respect to the host is steepest for those filters with larger increases in brightness, with the *Swift* $UVM2$ magnitude declining at a rate of roughly 3.5 magnitudes per 100 days. Table A1 contains all the follow-up photometric data.

2.3 New Spectroscopic Observations

We obtained seven low- and medium-resolution optical spectra of ASASSN-14ae spanning more than four months between 2014 January 29 and 2014 June 6. The spectra were obtained with DIS mounted on the Apache Point Observatory 3.5-m telescope (range 3500 − 9800 Å, R ∼ 1000) and with the Multi-Object Double Spectrographs (MODS; Pogge et al. 2010) on the 8.4-m Large Binocular Telescope (LBT) on Mount Graham (range 3200−10000 Å, R ∼ 2000). The spectra from DIS were reduced using standard techniques in IRAF and the spectra from MODS were reduced

[2] We also attempted to do image subtraction with the SDSS archival images as templates. However, due to the lack of stars in the field-of-view close to ASASSN-14ae, the quality of the subtractions was sub-optimal.

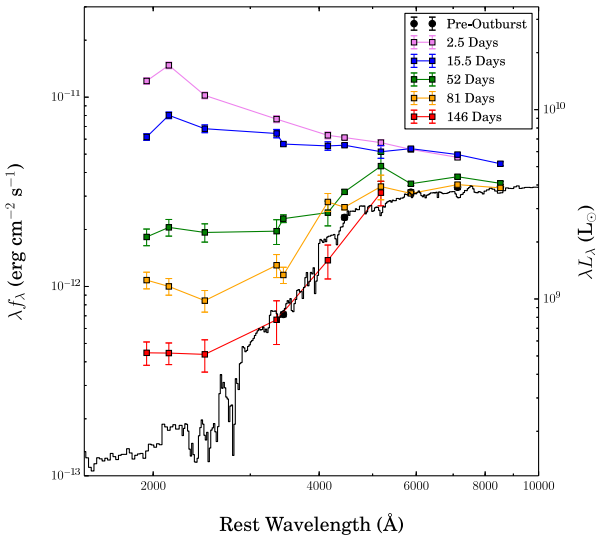

Figure 3. Observed spectral energy distribution of ASASSN-14ae and its host galaxy. The colored squares show the SED of ASASSN-14ae at the different epochs noted in the legend (listed as days since discovery). The black circles show archival SDSS *ugriz* data and the black line shows the best-fit host galaxy SED from FAST. All fluxes have been corrected for Galactic extinction and all data points include error bars, although they can be smaller than the data points.

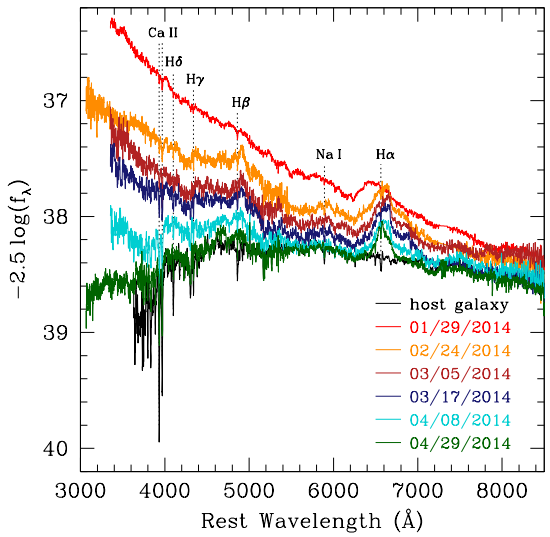

Figure 4. Spectral time-sequence of ASASSN-14ae during the outburst. Each spectrum shows the UT date it was obtained. Also plotted is the archival SDSS host spectrum, in black. Absorption features from the host galaxy are identified with black dotted lines. The transient spectra continue to show prominent broad Hα emission at all epochs, as well as other Balmer lines.

using a custom pipeline written in IDL[3]. We applied telluric corrections to all the spectra using the spectrum of the spectrophotometric standard observed the same night. We calculated synthetic r-band magnitudes and scaled the fluxes in each spectrum to match the r-band photometry. Figure 4 shows a montage of the flux-calibrated spectra from both DIS and MODS, while Figure 5 shows the same six spectra with the host galaxy spectrum subtracted.

The main characteristics of the spectra of ASASSN-14ae are the blue continuum, consistent with the photometric measurements, and the detection of broad Balmer lines in emission, which are not present in the host galaxy spectrum. The Hα line has FHWM $\gtrsim 8000$ km s^{-1} at all epochs and does not show a P-Cygni absorption trough. The blue continuum present in the first follow-up spectrum from 2014 January 29 becomes progressively weaker over time, with the spectrum from 2014 April 29 showing only slight emission above the host at wavelengths shorter than ~ 4000 Å. While the latest spectrum from 2014 June 6 appears to show more blue continuum emission than the previous epoch, the flux calibration and host subtraction for this spectrum are uncertain, and the corresponding *Swift* photometry indicates the UV emission of the source should be fading. The broad Hα emission feature becomes stronger relative to the continuum (higher equivalent width) after the initial spectrum and continues to show strong emission in all later epochs. Other broad emission features can be seen as well, including a He II 4686 line which has become stronger in equivalent width relative to the Balmer lines in the latest spectrum. We further analyze the features of these spectra in comparison to SNe, AGN, and TDEs in §3.3.

3 ANALYSIS

3.1 Light Curve Analysis

After correcting both the host and transient fluxes for Galactic extinction, we produced host-subtracted light curves for all 9 photometric filters. From these data we calculate peak absolute magnitudes and decline rates for all *Swift* filters, which are reported in Table 2. Comparison with luminous supernovae SN 2008es (Miller et al. 2009) and SN 2009kf (Botticella et al. 2010), both of which had absolute V-band magnitudes roughly equal to or greater than that of ASASSN-14ae, shows that the UV decline rates of these highly luminous supernovae are much faster than what we observe for ASASSN-14ae, indicating that a supernova explanation for the event is disfavored.

ASASSN-14ae's UV-UV and UV-optical color evolution are also atypical of hydrogen-rich supernovae with broad lines. Figure 6 shows the full host-subtracted UV-UV and UV-U color evolution for ASASSN-14ae in all *Swift* filters and Figure 7 compares the $(UVM2 - UVW1)$ and $(UVM2 - U)$ colors to those of SN 2008es, a superluminous SN IIL (Miller et al. 2009; Gezari et al. 2009), and SN 2012aw, a normal SN IIP (Bayless et al. 2013), which were also heavily observed with *Swift*. For SN 2008es we applied cross-filter K-corrections to obtain the rest-frame colors assuming a blackbody with $T_{\rm eff} = 8000$ K (Miller et al. 2009; Gezari et al. 2009), but we did not apply these corrections to SN 2012aw or ASASSN-14ae as they are much lower redshift. ASASSN-14ae shows almost no change in $(UVM2 - UVW1)$ color and became only slightly redder in

[3] `http://www.astronomy.ohio-state.edu/MODS/Software/modsIDL/`

Table 2. Peak absolute magnitudes and estimated decline rates of ASASSN-14ae in *Swift* filters

Filter	Absolute Magnitude	Magnitude Uncertainty	Decline Rate (mag/100 days)	Decline Rate Uncertainty
V	−19.5	0.20	1.9	0.30
B	−19.4	0.07	3.6	0.36
U	−19.8	0.05	3.5	0.30
$UVW1$	−19.8	0.04	4.0	0.30
$UVM2$	−20.0	0.04	3.3	0.16
$UVW2$	−19.7	0.04	3.6	0.13

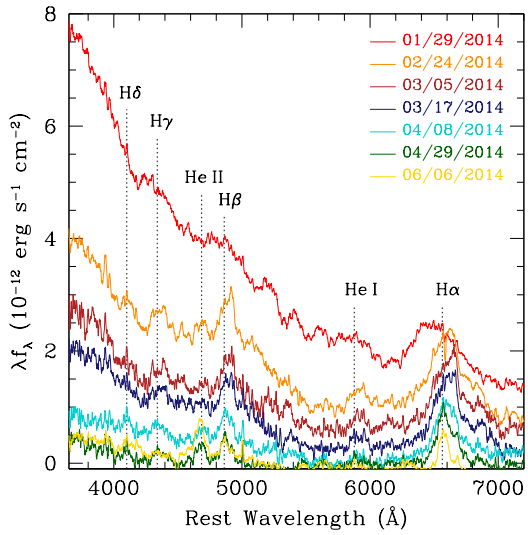

Figure 5. Host-galaxy-subtracted spectral time-sequence of ASASSN-14ae. Each spectrum shows the UT date it was obtained. Prominent emission features are identified with black dotted lines. The transient spectra show many broad emission features in all epochs, and blue continuum emission is still present at wavelengths shorter than $\sim$ 4000 Å in the latest spectrum from 2014 June 6. In later epochs, the He II 4686 line has become stronger relative to the Balmer lines

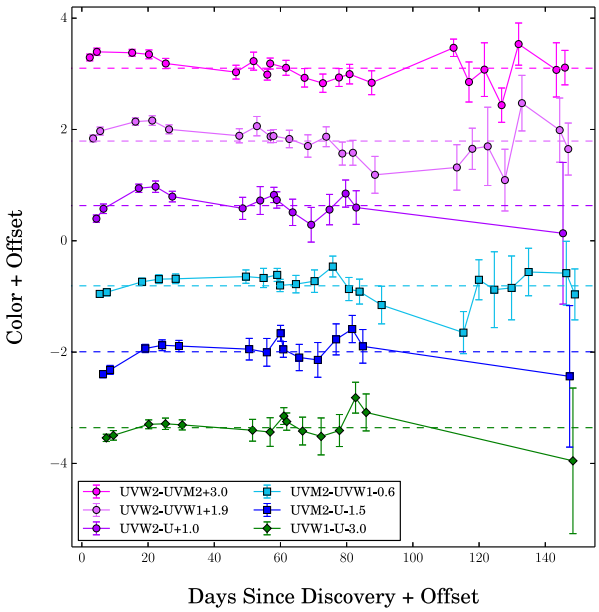

Figure 6. $(UV-UV)$ and $(UV-U)$ color evolution of ASASSN-14ae for all *Swift* UV bands. All fluxes used to calculate the colors shown were corrected for Galactic extinction and host-subtracted. $(UVW2-X)$ colors are shown as circles colored different shades of purple, $(UVM2-X)$ colors are shown as squares colored different shades of blue, and $(UVW1-U)$ is shown as diamonds and colored green. Each color term is offset in magnitude by a constant indicated in the legend and offset in epoch by 1 day from the term above it in order to make the plots easier to read. Horizontal dashed lines are centered on the average value of the color term plotted in the same color and are shown to aid the eye in seeing the general shape of the curves. ASASSN-14ae becomes slightly bluer in $(UVW2-X)$ colors and slightly redder in $(UVW1-U)$, but all terms show only slight evolution over the time shown.

$(UVM2-U)$ during the $\sim$ 80 days shown in the Figure. In contrast, SN 2008es became redder in both colors over time, while SN 2012aw became significantly redder in both colors over the first $\sim$ 20 days after discovery and then remained roughly constant in later epochs. ASASSN-14ae looks like neither of these, and all its $(UV-UV)$ and $(UV-U)$ colors show little change over the time shown in Figure 6, implying the most likely SN types that could produce the observed spectra of ASASSN-14ae are unlikely to be the sources of the transient.

3.2 SED Analysis

Using the host-subtracted fluxes of ASASSN-14ae we fit the transient SEDs with blackbody curves using Markov Chain Monte Carlo (MCMC) methods. The evolution of the source's SED along with the best-fit blackbody curves are shown in Figure 8. At early epochs, the blackbody fit is not able to replicate the apparent excess in the $UVM2$ (2246 Å) filter. This excess is not created by the extinction correction and corresponds to no obvious emission line. Using the best-fit blackbody curves we estimate the temperature and luminosity evolution of ASASSN-14ae. The derived estimates, along with 90% confidence errors and the χ^2 values of the best-fit blackbody curve, are given in Table 3 and shown in Figure 9. When there were *Swift* observations the temperature was estimated as a free parameter. When the UV data were not available, the temperature was constrained by a prior shown by the solid line in Figure 9 that roughly tracks the epochs with UV data. There are some degeneracies between the temperature and luminosity because much of the luminosity is farther in the UV than our data cover for these temperatures, resulting in relatively large uncertainties in some cases. In general, the temperature of the source falls from $T \sim 20,000$ K to $T \sim 15,000$ K during the first

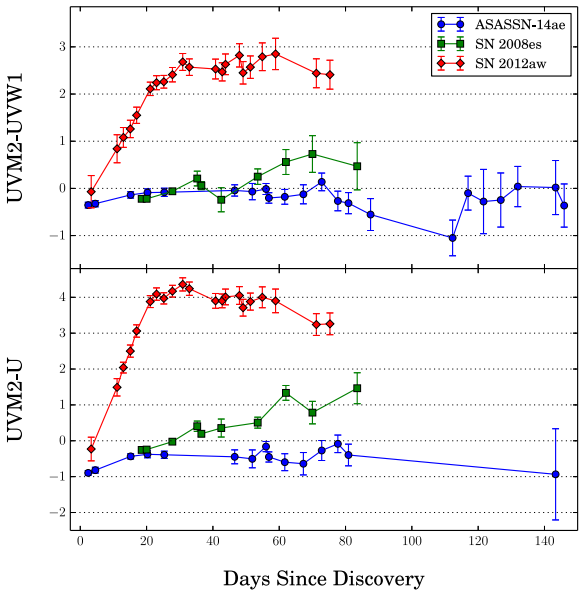

Figure 7. Comparison of $(UVM2 - UVW1)$ (top panel) and $(UVM2 - U)$ (bottom panel) color evolution between ASASSN-14ae (blue circles); SN 2008es, a super-luminous SN IIL (Gezari et al. 2009, green squares); and SN 2012aw, a SN IIP (Bayless et al. 2013, red diamonds). K-correction has been applied to the photometry for SN 2008es. ASASSN-14ae shows little evolution in either color while SN 2008es becomes redder in both colors and SN 2012aw becomes significantly redder over the first ~ 20 days after detection and remains roughly constant thereafter.

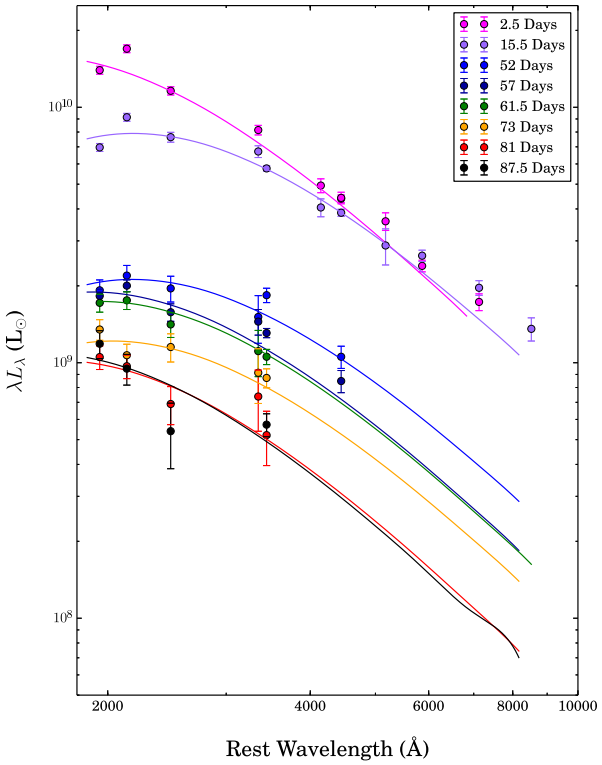

Figure 8. Evolution of the SED of ASASSN-14ae (shown in different colors) along with the best-fitting blackbody models for each epoch. Only epochs with both *Swift* and ground data taken within 0.5 days of each other and only data points with $f_{sub}/f_{host} \geq 0.3$ are shown. All data points have been extinction-corrected and include error bars, although they can be smaller than the data points. At early epochs, the blackbody fits are not able to replicate the apparent excess in the *Swift* $UVM2$ band.

~ 20 days of the outburst, then rises again to $T \sim 20,000$ K over the next ~ 50 days, and then remains roughly constant for the rest of the period shown. Conversely, the luminosity fades steadily over the 150-day period shown. Integrating over the luminosity curve using the epochs with directly estimated temperatures gives a value of $E \simeq 1.7 \times 10^{50}$ ergs for the total energy radiated by ASASSN-14ae during this time. This only requires accretion of $\Delta M \sim 10^{-3} \eta_{0.1}^{-1}$ M$_\odot$ of mass, where $\eta = 0.1\eta_{0.1}$ is the radiative efficiency.

After the first ~ 10 days, the luminosity evolution is well fit as an exponential $L \propto e^{-t/t_0}$ with $t_0 \simeq 39$ days as shown in Figure 9. This differs from most TDE models where the luminosity evolution is described as a power law t^{-x} with $x \simeq 5/12 - 5/3$ (e.g., Strubbe & Quataert 2009; Lodato & Rossi 2011). However, this temperature and luminosity behavior would be highly unusual for a supernova, which typically exhibit a temperature that drops considerably within days of the explosion along with either a relatively constant luminosity (Type IIP; e.g., Botticella et al. 2010) or a declining luminosity (Type IIn, IIL, Ic; e.g., Miller et al. 2009; Inserra et al. 2013; Graham et al. 2014).

While it is unlikely we are seeing direct emission from a thin disk, we can model the data using the surface brightness profile of a thin disk (Shakura & Sunyaev 1973). We make the disk infinite, where the location of the inner edge is unimportant given our wavelength coverage. Adding an outer edge could be used to make the profile rise more steeply towards shorter wavelengths. Figure 10 shows the implied luminosity of the disk in Eddington units, where the estimate of L/L_{Edd} depends on the black hole mass $M_{BH} = 10^6 M_{BH6} M_\odot$, the disk inclination factor $\cos i$ and the radiative efficiency $\eta = 0.1\eta_{0.1}$ in the sense that raising the black hole mass, making the disk inclined to the line of site or lowering the radiative efficiency will reduce the observed luminosity relative to the Eddington limit. In general, the SED of a thin disk fits the data significantly worse than a blackbody. Like the bolometric luminosity, the estimated thin disk luminosity drops exponentially with time rather than as a power law, following a plateau at $L/L_{Edd} \simeq 10\eta_{0.1} M_{BH6}^{-2} \cos^{-3/2} i$ for the first ~ 20 days. Raising the black hole mass scale to $M_{BH} \sim 10^{6.5}$ M$_\odot$ would allow $L/L_{Edd} \sim 1$ at peak. The differences compared to the Eddington limit shown in Figure 9 arise from the enormous increase in the unobserved hard UV emission which we discuss in §3.3 using the broad emission lines.

3.3 Spectral Analysis

The spectra of ASASSN-14ae show broad Balmer lines in emission with a blue continuum, including an important contribution of the host galaxy (especially in the red) at late times (see Figure 4). We subtracted the SDSS host galaxy spectrum from ASASSN-14ae spectra in order to compare to other objects and for analyzing the spectral line profiles. Figure 11 shows a comparison of ASASSN-14ae host-subtracted spectra at two different epochs after discovery with the spec-

Table 3. ASASSN-14ae blackbody Evolution

MJD	Best-Fit χ^2	Luminosity (10^9 $L_\odot$)	Temperature (10^4 K)	Radius (10^{14} cm)
56684.6	35.5	21.6 ± 1.3	2.2 ± 0.1	7.0 ± 0.3
56697.4	37.2	10.7 ± 0.4	1.6 ± 0.0	9.3 ± 0.5
56698.5	27.0	9.3 ± 0.8	1.5 ± 0.1	10.4 ± 0.8
56728.6	9.8	3.1 ± 0.2	1.6 ± 0.1	5.3 ± 0.6
56734.2	15.0	2.9 ± 0.2	1.6 ± 0.1	4.8 ± 0.6
56739.6	17.2	2.6 ± 0.2	1.9 ± 0.2	3.4 ± 0.5
56744.1	1.7	2.3 ± 0.2	1.9 ± 0.2	3.1 ± 0.4
56755.2	32.1	1.7 ± 0.2	1.7 ± 0.2	3.1 ± 0.5
56763.2	9.7	1.4 ± 0.4	2.1 ± 0.5	1.9 ± 0.7
56770.3	18.2	1.5 ± 0.4	2.2 ± 0.4	1.9 ± 0.4
56794.8	28.4	0.8 ± 0.1	2.0 ± 0.2	1.7 ± 0.3

The results are given only for epochs with *Swift* data, where the temperature can be estimated without a prior.

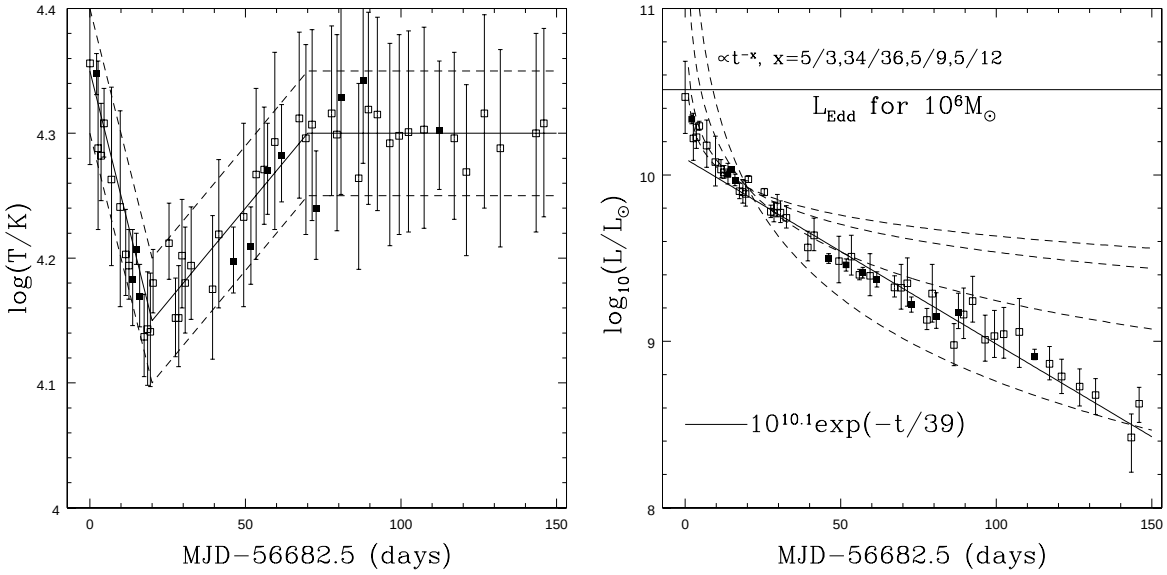

Figure 9. *Left Panel*: Evolution of ASASSN-14ae's blackbody temperature with temperatures fit with a prior (open points) and without a prior (filled points). The horizontal lines show our temperature prior, with the solid line showing our central temperature prior and the dashed lines showing the 1σ spread in the prior. The temperature of the source falls from $T \sim 20,000$ K to $T \sim 15,000$ K during the first ~ 20 days of the outburst, then rises again to $T \sim 20,000$ K over the next ~ 50 days before remaining roughly constant for the rest of the period shown. *Right Panel*: Evolution of ASASSN-14ae's luminosity over time. Dashed lines show popular power law fits for TDE luminosity curves $L \propto t^{-x}$ (e.g., Strubbe & Quataert 2009; Lodato & Rossi 2011) while the diagonal solid line shows an exponential fit. The solid horizontal line shows the Eddington luminosity for a $M = 10^6$ $M_\odot$ black hole. The exponential model appears to fit the luminosity curve of ASASSN-14ae better than any of the power law fits typically used for TDEs.

tra of SNe II (SN 2010jl, ASASSN-13co, and SN 2008es) and a broad-line AGN (SDSS J1540-0205). SN 2010jl is a luminous SN IIn ($M_V \simeq -20$ mag, Stoll et al. 2011), SN 2008es is a super-luminous SN IIL ($M_V \simeq -22$ mag, Miller et al. 2009), and ASASSN-13co is a luminous SN IIP ($M_V \simeq -18$ mag, Holoien et al. 2013). At the earliest epoch, the spectrum of ASASSN-14ae is similar to ASASSN-13co and SN 2008es, dominated by a blue continuum. At the later epoch, the spectrum of ASASSN-14ae stays blue, but the spectra of the SN II ASASSN-13co and SN 2008es become significantly redder, consistent with the comparison in color evolution illustrated in Figure 7. The spectral lines also show differences. In ASASSN-14ae the Hα is broad (FWHM $\gtrsim 8,000$ km s^{-1}) at all times and does not show the P-Cygni profile that is characteristic of SNe II with broad lines. The spectrum of ASASSN-14ae is quite different from the Type IIn SN 2010jl (Stoll et al. 2011; Zhang et al. 2012) at early and late times, both in line profiles (SNe IIn have narrower lines with FWHM $\lesssim 5,000$ km s^{-1}) and continuum shape. The spectrum of the low-ionization broad-line AGN SDSS J1540-0205 (Strateva et al. 2003) does not resemble the spectrum of ASASSN-14ae in the earlier epoch but shows interesting similarities with the spectrum of ASASSN-14ae at 50 days after discovery. In particular, it has a complex Hα line profile, which is thought to be produced by emission from the accretion disk (Strateva et al. 2003).

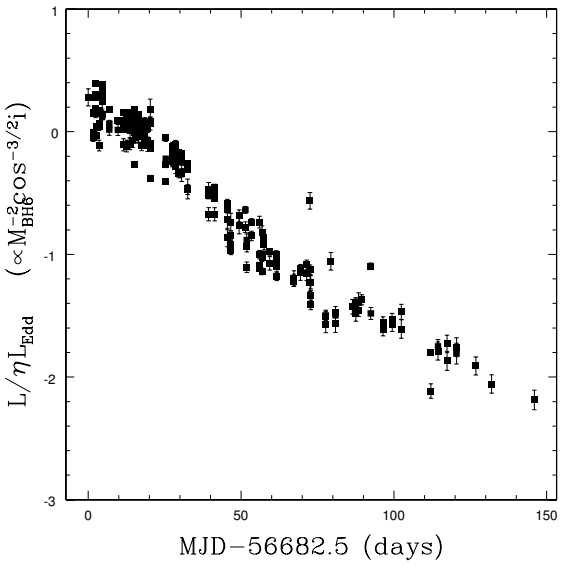

Figure 10. Implied luminosity in Eddington units of ASASSN-14ae using a thin disk model. The estimated L/L_{Edd} depends on the black hole mass $M_{BH} = 10^6 M_{BH6}$ $M_\odot$, the disk inclination factor $\cos i$ and the radiative efficiency $\eta = 0.1\eta_{0.1}$. Raising the black hole mass scale to $M_{BH} \sim 10^{6.5}$ $M_\odot$ would produce $L/L_{Edd} \sim 1$ at peak. In general, the SED of the thin disk fits the data significantly worse than a blackbody (see Figure 13 below).

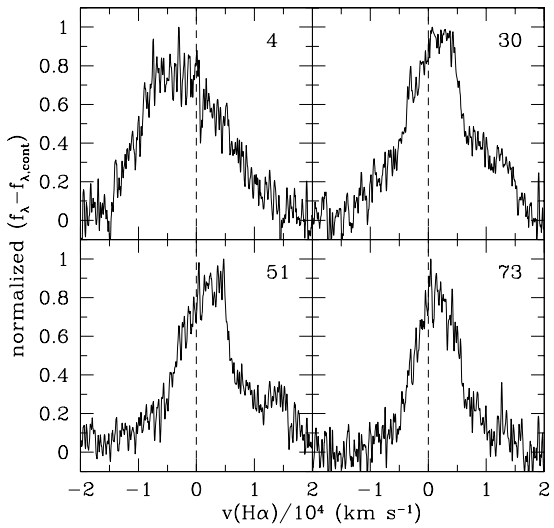

Figure 12. Evolution of the Hα line profile of ASASSN-14ae as a function of time. We have subtracted the host galaxy spectrum and a low-order continuum defined locally around the line. The days since discovery are shown in the top-right part of each panel. The integrated luminosity of the Hα line is $L_{H\alpha} \simeq 2.7 \times 10^{41}$ erg s^{-1} at four days, $L_{H\alpha} \simeq 3.3 \times 10^{41}$ erg s^{-1} at 30 days, $L_{H\alpha} \simeq 3.2 \times 10^{41}$ erg s^{-1} at 51 days, and $L_{H\alpha} \simeq 2.1 \times 10^{41}$ erg s^{-1} at 70 days.

In Figure 12 we show the evolution of the Hα line profile of ASASSN-14ae as a function of time. In the first epoch, 4 days after discovery, the line can be well-fit with a Gaussian profile centered at $v_{peak} \sim -3,000$ km s^{-1} and with FWHM $\simeq 17,000$ km s^{-1} and integrated luminosity $L_{H\alpha} \simeq 2.7 \times 10^{41}$ erg s^{-1}. However, the line peak evolves to the red and the shape becomes significantly asymmetric in later epochs between $\sim 30 - 50$ days after discovery. The peak of the profile in these epochs is at $v_{peak} \sim 3,000 - 4,000$ km s^{-1} and the blue/red wing of the line reaches $\sim -15,000/+20,000$ km s^{-1}, showing a strong red asymmetry. At 70 days after discovery, the profile again becomes more symmetric and can be relatively well-fit using a gaussian with $v_{peak} \sim +1,400$ km s^{-1} , FWHM $\simeq 10,000$ km s^{-1} and integrated luminosity $L_{H\alpha} \simeq 2.1 \times 10^{41}$ erg s^{-1}. In the spectrum from 2014 April 29, not shown in Figure 12, the Hα line has FWHM $\simeq 8,000$ km s^{-1} and its integrated luminosity has only decreased by a factor of three since the first epoch, to $L_{H\alpha} \simeq 1.2 \times 10^{41}$ erg s^{-1}. In the April 29 spectrum we also detect broad He II 4686 with FWHM $\simeq 6,000$ km s^{-1} and $L_{HeII} \simeq 3 \times 10^{40}$ erg s^{-1}. In the latest spectrum from 2014 June 6, this He II line has become stronger relative to the Balmer lines, but has the same FWHM.

In summary, the spectra of ASASSN-14ae seem to be inconsistent with the spectra of SN II and the Hα emission line profile shows strong evolution during the event. Compared to the spectra of TDEs in the literature, the most similar to ASASSN-14ae is SDSS TDE2 (van Velzen et al. 2011), which showed a broad Hα line with FWHM $\simeq 8,000$ km s^{-1}. The spectra of PS1-10jh (Gezari et al. 2012) showed a He II 4686 line in emission with FWHM $\simeq 9,000$ km s^{-1} and the spectra of PS1-11af (Chornock et al. 2014) did not show any emission lines. The recent paper by Arcavi et al. (2014) presents spectra of multiple TDE candidates and shows that their spectra fall on a continuum, with some events being more He-rich and others being more H-rich. The spectra of ASASSN-14ae resembles the other TDE candidates, and with both strong He and H emission, it appears to fall in the middle of the proposed continuum of spectral properties.

If we assume that the Hα and He II emission are driven by photoionization and recombination, we can gain some insight into the hard UV continuum and the physical conditions of the line emitting region. In particular, if α_B and α_l are the case B recombination and line emission rate coefficients, and E_i and E_l are the energies of the ionization edge and the line, then we can estimate the luminosity at the ionization edge as $L_i = L_l(\alpha_B/\alpha_l)(E_i/E_l)$, which for $L_{H\alpha} \simeq 2 \times 10^{41}$ and $L_{HeII} \simeq 3 \times 10^{40}$ erg s^{-1} implies ionizing luminosities of 3×10^{42} and 2×10^{41} erg s^{-1}, respectively, as shown in Figure 13. If we compare these estimates, we see that the SED probably requires some additional hard UV emission beyond that expected from the blackbody fits, but definitely has a sharp cutoff at wavelengths only somewhat shorter than the blackbody predictions. This assumes an emission line gas covering fraction $\epsilon \simeq 1$ near unity, and these ionizing luminosities can be shifted upwards as ϵ^{-1}. However, the covering fractions for H and He are unlikely to differ enormously, so the SED likely must fall towards shorter wavelengths independent of the exact value of ϵ. This is also consistent with the X-ray flux limit from §2.2.

For comparison, Figure 13 shows the SED of a thin disk, raising the black hole mass to $M_{BH} = 10^{6.5} M_\odot$ so that an $L/L_{Edd} \simeq 1$ disk with efficiency $\eta = 0.1$ is consistent with the observed UV emission near MJD 56729 (as compared

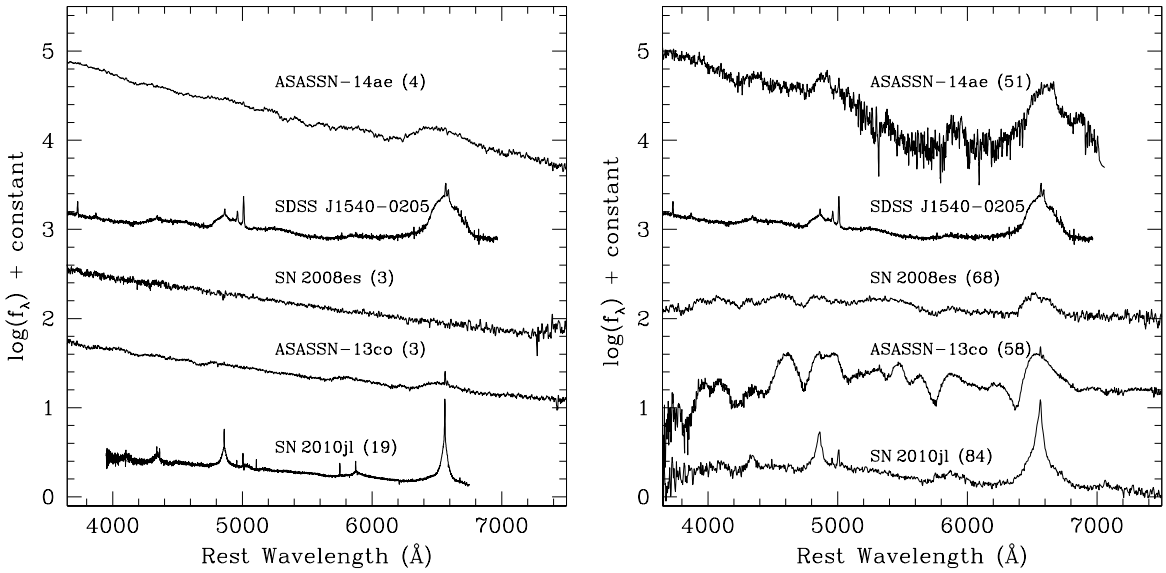

Figure 11. Comparison of the host-subtracted spectra of ASASSN-14ae with the spectra of the Type IIn SN 2010jl (Stoll et al. 2011; Zhang et al. 2012), the Type IIL SN 2008es (Miller et al. 2009), the Type IIP ASASSN-13co (Holoien et al. 2013), and the broad-line AGN SDSS J1540-0205 (Strateva et al. 2003). The left panel shows the spectra at an early phase and the right panel at a later phase with respect to discovery or maximum light (except for the AGN). The days with respect to maximum light (SN 2008es, SN 2010jl) or discovery (ASASSN-14ae, ASASSN-13co) are shown in parenthesis, next to the names of the transients.

with Figure 10). The inner regions of the disk are much hotter than the blackbody, so the SED continues to rise into the hard UV, producing far more ionizing flux than is required. This is true even when we add an inner edge at $R_{in} = 3r_g$ where $r_g = GM_{BH}/c^2$ is the gravitational radius of the black hole. Thus, while there must be some excess hard emission compared to a blackbody, it is likely less than for a thin disk. Note that the effects of the inner disk edge only affect the very hard UV and X-ray emission, which is why we could ignore the inner edge in the SED models from §3.2. The different shape of the thin disk model where we have the optical and near-UV SED also shows why the blackbody models are a better fit to the directly observed SEDs. Extrapolating the SED following the thin disk model would increase the total energy budget and accreted mass by roughly an order of magnitude.

We can also estimate the gas mass associated with the line emission if we assume that the line widths are related to orbital velocities. The emission radius for a velocity of $v = 5000v_5$ km/s is of order

$$r_\alpha \simeq 5 \times 10^{14} M_{BH6} v_5^{-2} \text{ cm} \quad (1)$$

and the Hα luminosity is of order

$$L_{H\alpha} \simeq \frac{4\pi}{3} r_\alpha^3 n^2 \alpha_l E_l \quad (2)$$

where α_l and E_l are the volumetric rate and line energy and we assume a spherical geometry. This implies a characteristic number density of order

$$n \simeq 3 \times 10^{10} L_{\alpha 41}^{1/2} v_5^3 M_{BH6}^{-3/2} \text{ cm}^{-3} \quad (3)$$

which implies that the line emission should almost instantaneously track the hard UV emission because the recombination times are short. The mass associated with the emission line region is then

$$M_\alpha \simeq 0.016 L_{\alpha 41}^{1/2} M_{BH6}^{3/2} v_5^{-3} M_\odot \quad (4)$$

which is an order of magnitude larger than the amount of accreted mass needed to power the transient.

4 DISCUSSION

The transient ASASSN-14ae, discovered by ASAS-SN on 2014 January 25, had a peak absolute V-band magnitude of $M_V \sim -19.5$ and position consistent to within 0.09 ± 0.14 arcseconds of the center of SDSS J110840.11+340552.2. However, it does not appear to be consistent with either a supernova or a normal AGN outburst. Its colors remain blue over 140 days since detection, rather than showing the rapid reddening seen in super-luminous SNe with similar absolute magnitudes, and ASASSN-14ae's temperature has remained relatively constant at $T \sim 20,000$ K for the duration of the outburst while declining steadily in luminosity at a rate best fit by an exponential decay curve, behavior which is inconsistent with nearly all SNe. Finally, spectra of ASASSN-14ae show a strong blue continuum and broad emission features, including Balmer lines and a He II line, and its spectral evolution does not appear to match either those of SNe or AGN. While highly unusual AGN activity or a strange SN cannot be ruled out completely, the observational characteristics of ASASSN-14ae disfavor both of these scenarios.

Archival photometry, spectroscopy, and SED fitting indicate that SDSS J110840.11+340552.2 appears to be an early-type galaxy with a generally intermediate-to-old-aged stellar population but some signs of recent star formation. While the recent star formation indicates that the galaxy

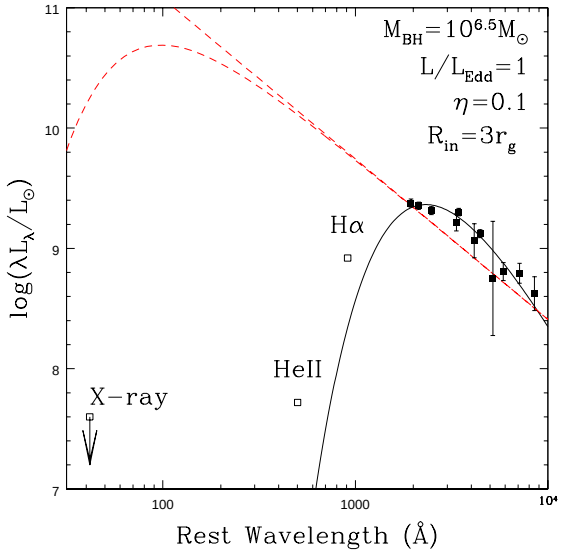

Figure 13. SED of a thin disk with the black hole mass raised to $M_{BH} = 10^{6.5} M_\odot$ so that a disk radiating at the Eddington luminosity is consistent with the observed UV emission from MJD 56729 without an inner edge (straight red dashed line), and with an inner edge at $R_{in} = 3r_g$ (curved red dashed line). Both models rise into the hard UV, producing far more ionizing flux than is required to produce the observed Hα and He II emission (unfilled boxes). The X-ray limit shown is based on *Swift* XRT data collected through 2014 April 24; including later data would make this limit tighter, as discussed in §2.2. These estimates of the ionizing luminosity can be shifted to higher luminosities as the inverse of the covering fraction, but H and He probably have to be shifted by similar amounts, which would imply that the spectrum must still be falling towards shorter wavelengths.

could host a core-collapse SN, the supernova explanation is disfavored by photometric and spectroscopic observations, as previously mentioned. SDSS J110840.11+340552.2 shows spectral emission features indicating only a weak AGN host at best, and its mid-IR colors from WISE are inconsistent with significant AGN activity, further disfavoring normal AGN activity as an explanation for ASASSN-14ae.

Conversely, many of the observed properties of ASASSN-14ae are consistent with other TDE candidates discussed in the literature. The blue colors, slow decline rate, and color evolution have been seen in many TDE candidates, and these transients are predicted to show a largely constant temperature and steadily declining luminosity curve. ASASSN-14ae's spectra also do not appear to be highly unusual for TDEs, and in fact are a very close match to spectra of the SDSS candidate TDE 2 (van Velzen et al. 2011) and the PTF candidate PTF09djl (Arcavi et al. 2014). With both strong He and H emission lines, ASASSN-14ae appears to fall in the middle of the He-rich-to-H-rich continuum proposed by Arcavi et al. (2014).

Thus, we conclude that ASASSN-14ae is probably a TDE. ASASSN-14ae appears to be the lowest redshift candidate TDE discovered at optical or UV wavelengths, and continues to emit well above host galaxy levels in the UV over 140 days since discovery. In the most recent spectra, the optical continuum is again dominated by the host, but with a prominent, broad Hα line and other, weaker Balmer and He II lines.

The amount of mass associated with the event is small, roughly 10^{-3} $M_\odot$ of accreted material is sufficient to power the transient, and $\sim 10^{-2}$ $M_\odot$ is associated with the line emission region. This suggests that this event is likely powered by tidally stripping the envelope of a giant rather than by the complete disruption of a main-sequence star, as described in MacLeod, Guillochon, & Ramirez-Ruiz (2012), similar to the case seen with black hole candidate ESO 243-49 HLX-1 (Webb et al. 2014). The duration of a TDE can be truncated by putting the star on an orbit bound to the black hole (Hayasaki et al. 2013), but this necessarily implies that a larger fraction of the stellar mass is on bound orbits and so should enhance the total energy release. On the other hand, disruptions of giants on parabolic orbits have the same asymptotic $t^{-5/3}$ power law for the rate of return of material to pericenter, but they have a far higher peak. At its simplest, a constant density spherical star has a return rate proportional to $P^{-5/3}(1-(P/P_0)^{4/3})$ where P_0 is the period at the surface, while a shell has a rate simply proportional to $P^{-5/3}$ for $P > P_0$ in both cases. As a result, disruptions of giant envelopes should show both faster rises and declines.

The fact that ASAS-SN has discovered a likely TDE in the first year of real-time operations, despite only having two cameras operational during most of this period, indicates that we may find these events on a yearly basis now that we are operational in both the Northern and Southern hemispheres. Using the estimates for the local density of black holes from Shankar (2013) and an observable volume of 3×10^7 Mpc^3 expected for the fully operational (both hemispheres) ASAS-SN gives a total of $\sim 3 \times 10^4$ black holes with masses in the $M_{BH} = 10^6 - 10^7$ $M_\odot$ mass range that will be observable by ASAS-SN. Given a TDE rate of $(1.5-2.0)^{+2.7}_{-1.3} \times 10^{-5}$ yr^{-1} per galaxy (van Velzen & Farrar 2014), and assuming a 50% detection efficiency, we calculate an expected rate of roughly $0.1 - 0.7$ TDEs per year to be found in ASAS-SN data. Using the volumetric TDE rate from the same manuscript of $(4-8) \times 10^{-8\pm0.4}$ yr^{-1}Mpc^{-3} gives a more optimistic rate of $0.3 - 3$ TDEs per year to be found in ASAS-SN data. These nearby events will be easily observable with a variety of telescopes and instruments, allowing us to study these TDEs across a broad wavelength range and at a level that cannot be done for TDEs discovered at higher redshifts. This will allow us to develop a catalog of well-observed TDE candidates that can be used for population studies, and if candidates are caught early enough, to examine the early behavior of these events. Although ASAS-SN is focused primarily on the discovery and observation of supernovae, it will also be an invaluable resource for studying TDEs and other bright transients in the future.

ACKNOWLEDGMENTS

The authors thank A. Piro, F. Shankar, N. McConnell, M. Strauss, J. Greene, and J. Guillochon for useful comments and suggestions. We thank M. L. Edwards and the staff of the LBT Observatory for their support and assistance in obtaining the MODS spectra. We thank PI Neil Gehrels and

the *Swift* ToO team for promptly approving and executing our observations. We thank LCOGT and its staff for their continued support of ASAS-SN.

Development of ASAS-SN has been supported by NSF grant AST-0908816 and the Center for Cosmology and AstroParticle Physics at the Ohio State University. JFB is supported by NSF grant PHY-1101216.

This research has made use of the XRT Data Analysis Software (XRTDAS) developed under the responsibility of the ASI Science Data Center (ASDC), Italy. At Penn State the NASA *Swift* program is support through contract NAS5-00136.

The LBT is an international collaboration among institutions in the United States, Italy and Germany. LBT Corporation partners are: The University of Arizona on behalf of the Arizona university system; Istituto Nazionale di Astrofisica, Italy; LBT Beteiligungsgesellschaft, Germany, representing the Max-Planck Society, the Astrophysical Institute Potsdam, and Heidelberg University; the Ohio State University, and The Research Corporation, on behalf of The University of Notre Dame, University of Minnesota and University of Virginia.

This publication used data obtained with the MODS spectrographs built with funding from NSF grant AST-9987045 and the NSF Telescope System Instrumentation Program (TSIP), with additional funds from the Ohio Board of Regents and the Ohio State University Office of Research.

The Liverpool Telescope is operated on the island of La Palma by Liverpool John Moores University in the Spanish Observatorio del Roque de los Muchachos of the Instituto de Astrofisica de Canarias with financial support from the UK Science and Technology Facilities Council.

This research was made possible through the use of the AAVSO Photometric All-Sky Survey (APASS), funded by the Robert Martin Ayers Sciences Fund.

Funding for SDSS-III has been provided by the Alfred P. Sloan Foundation, the Participating Institutions, the National Science Foundation, and the U.S. Department of Energy Office of Science. The SDSS-III web site is http://www.sdss3.org/.

SDSS-III is managed by the Astrophysical Research Consortium for the Participating Institutions of the SDSS-III Collaboration including the University of Arizona, the Brazilian Participation Group, Brookhaven National Laboratory, Carnegie Mellon University, University of Florida, the French Participation Group, the German Participation Group, Harvard University, the Instituto de Astrofisica de Canarias, the Michigan State/Notre Dame/JINA Participation Group, Johns Hopkins University, Lawrence Berkeley National Laboratory, Max Planck Institute for Astrophysics, Max Planck Institute for Extraterrestrial Physics, New Mexico State University, New York University, Ohio State University, Pennsylvania State University, University of Portsmouth, Princeton University, the Spanish Participation Group, University of Tokyo, University of Utah, Vanderbilt University, University of Virginia, University of Washington, and Yale University.

This publication makes use of data products from the Two Micron All Sky Survey, which is a joint project of the University of Massachusetts and the Infrared Processing and Analysis Center/California Institute of Technology, funded by the National Aeronautics and Space Administration and the National Science Foundation.

This publication makes use of data products from the Wide-field Infrared Survey Explorer, which is a joint project of the University of California, Los Angeles, and the Jet Propulsion Laboratory/California Institute of Technology, funded by the National Aeronautics and Space Administration.

This research has made use of the NASA/IPAC Extragalactic Database (NED), which is operated by the Jet Propulsion Laboratory, California Institute of Technology, under contract with the National Aeronautics and Space Administration.

REFERENCES

Ahn C. P., Alexandroff R., Allende Prieto C., et al., 2012, ApJS, 203, 21
Arcavi I., Gal-Yam A., Sullivan M., et al., 2014, arXiv:1405.1415
Assef R. J., Stern D., Kochanek C. S., et al., 2013, ApJ, 772, 26
Bayless A. J., Pritchard T. A., Roming P. W. A., et al., 2013, ApJ, 764, L13
Bloom J. S., Giannios D., Metzger B. D., et al., 2011, Science, 333, 203
Botticella M. T., Trundle C., Pastorello A., et al., 2010, ApJL, 717, L52
Brandt W. N., Pounds K. A. & Fink H., 1995, MNRAS, 273, L47
Breeveld A. A., Curran P. A., Hoversten E. A., et al., 2010, MNRAS, 406, 1687
Brown T. M., Baliber N., Bianco F. B., et al., 2013, PASP, 125, 1031
Bruzual G. & Charlot S., 2003, MNRAS, 344, 1000
Burrows D. N., Hill J. E., Nousek J. A., et al., 2005, SSR, 120, 165
Burrows D. N., Kennea J. A., Ghisellini G., et al., 2011, Nature, 476, 421
Cardelli J. A., Clayton G. C., & Mathis J. S., 1988, ApJL, 329, L33
Cenko S. B., Bloom J. S., Kulkarni S. R., et al., 2012a, MNRAS, 420, 2684
Cenko S. B., Krimm H. A., Horesh A., et al., 2012b, ApJ, 753, 77
Chambers K. C., 2007, in American Astronomical Society Meeting Abstracts, 142.06
Chornock R., Berger E., Gezari S., et al., 2014, ApJ, 780, 44
Donato D., Cenko S. B., Covino S., et al., 2014, ApJ, 781, 59
Evans C. R. & Kochanek C. S., 1989, ApJL, 346, L13
Gezari S., Basa S., Martin D. C., et al., 2008, ApJ, 676, 944
Gezari S., Heckman T., Cenko S. B., et al., 2009, ApJ, 698, 1367
Gezari S., Chornock R., Rest A., et al., 2012, Nature, 485, 217
Graham A. W., Erwin P., Caon N., et al., 2001, ApJL, 563, L11

Graham M. L., Sand D. J., Valenti S., et al., 2014, arXiv:1402.1765
Grupe D., Beuermann K., Mannheim K., et al., 1995, AAP, 299, L5
Guillochon J., Manukian H. & Ramirez-Ruiz E., 2014, ApJ, 783, 23
Gültekin K., Richstone D. O., Gebhardt K., et al., 2009, ApJ, 698, 198
Hayasaki K., Stone N., & Loeb A., 2013, MNRAS, 434, 909
Hill J. E., Burrows D. N., Nousek J. A., et al., 2004, in Flanagan K. A., Siegmund O. H. W., eds, Society of Photo-Optical Instrumentation Engineers (SPIE) Conference Series Vol. 5165, X-Ray and Gamma-Ray Instrumentation for Astronomy XIII, 217
Holoien T. W.-S., Brimacombe J., Shappee B. J., et al., 2013, The Astronomer's Telegram, 5346, 1
Holoien T. W.-S., Prieto J. L., Stanek K. Z., et al., 2014, ApJL, 785, L35
Inserra C., Smartt S. J., Jerkstrand A., et al., 2013, ApJ, 770, 128
Kalberla P. M. W., Burton W. B., Hartmann D., et al., 2005, A&A, 400, 775
Kato T., Hambsch F., Masi G., et al., 2013, arXiv:1310.7069
Kochanek C. S., 1994, ApJ, 422, 508
Komossa S. & Bade N., 1999, AAP, 343, 775
Kraft R. P., Burrows D. N. & Nousek J. A., 1991, ApJ, 374, 344
Kriek M., van Dokkum P. G, Labbé I., et al., 2009, ApJ, 700, 221
Lacy J. H., Townes C. H., Hollenbach D. J., 1982, ApJ, 262, 120
Law N. M., Kulkarni S. R., Dekany R. G., et al., 2009, PASP, 121, 1395
Levan A. J., Tanvir N. R., Cenko S. B., et al., 2011, Science, 333, 199
Lodato G. & Rossi E. M., 2011, MNRAS, 410, 359
Loeb A. & Ulmer A., 1997, ApJ, 489, 573
MacLeod M., Guillochon J., & Ramirez-Ruiz E., 2012, ApJ, 757, 134
McConnell N. J. & Ma C.-P., 2013, ApJ, 764, 184
Mendel J. T., Simard L., Palmer M., et al., 2014, ApJS, 210, 3
Miller A. A., Chornock R., Perley D. A., et al., 2009, ApJ, 690, 1303
Phinney E. S., 1989, Nature, 340, 595
Pogge R. W., Atwood B., Brewer D. F., et al., 2010, in Society of Photo-Optical Instrumentation Engineers (SPIE) Conference Series, 7735, 77350
Poole T. S., Breeveld, A. A. and Page, M. J., et al., 2008, MNRAS, 383, 627
Prieto J. L., Bersier D., Holoien T. W.-S., et al., 2014, The Astronomer's Telegram, 5831, 1
Rees M. J., 1988, Nature, 333, 523
Roming P. W. A., Kennedy T. E., Mason K. O., et al., 2005, SSR, 120, 95
Schlafly E. F. & Finkbeiner D. P., 2011, ApJ, 737, 103
Schmidt S. J., Prieto J. L., Stanek K. Z., et al., 2014, ApJL, 781, L24
Shakura N. I. & Sunyaev R. A., 1973, AAP, 24, 337
Shankar F., 2013, Classical and Quantum Gravity, 30, 244001
Shappee B. J., Prieto J. L., Grupe D., et al., 2013, arXiv:1310.2241
Skrutskie M. F., Cutri R. M., Stiening R., et al., 2006, AJ, 131, 1163
Stanek K. Z., Shappee B. J., Kochanek C. S., et al., 2013, The Astronomer's Telegram, 5118, 1
Steele I. A., Smith R. J., Rees P. C., et al., 2004, in Oschmann Jr. J. M., ed., Society of Photo-Optical Instrumentation Engineers (SPIE) Conference Series Vol. 5489, Ground-based Telescopes, 679
Stoll R., Prieto J. L., Stanek K. Z., et al., 2011, ApJ, 730, 34
Strateva I. V., Strauss M. A., Hao L., et al., 2003, AJ, 126, 1720
Strubbe L. E. & Quataert E., 2009, MNRAS, 400, 2070
Ulmer A., 1999, ApJ, 514, 180
van Velzen S., Farrar G. R., Gezari S., et al., 2011, ApJ, 741, 73
van Velzen S., & Farrar G. R., 2014, arXiv:1407.6425
Voges W., et al., 1999, AAP, 349, 389
Webb N. A., Godet O., Wiersema K., et al., 2014, ApJL, 780, L9
Wright E. L., Eisenhardt P. R. M., Mainzer A. K., et al., 2010, AJ, 140, 1868
Zauderer B. A., Berger E., Soderberg A. M., et al., 2011, Nature, 476, 425
Zhang T., Wang X., Wu C., et al., 2012, AJ, 144, 131

APPENDIX A: FOLLOW-UP PHOTOMETRY

All follow-up photometry is presented in Table A1 below. Photometry is presented in the natural system for each filter: *ugriz* magnitudes are in the AB system, while *Swift* filter magnitudes are in the Vega system.

Table A1. Photometric data of ASASSN-14ae. Magnitudes are presented in the natural system for each filter: *ugriz* magnitudes are in the AB system, while *Swift* filter magnitudes are in the Vega system.

MJD	Filter	Magnitude	Magnitude Uncertainty	Telescope
56686.07742	z	16.147	0.022	LT
56694.00965	z	16.145	0.027	LT
56695.05779	z	16.149	0.025	LT
56696.15246	z	16.141	0.027	LT
56697.01584	z	16.130	0.033	LT
56698.03157	z	16.120	0.026	LT
56698.97949	z	16.115	0.028	LT
56699.95359	z	16.146	0.023	LT
56700.97094	z	16.135	0.030	LT
56701.93490	z	16.146	0.027	LT
56710.02390	z	16.190	0.028	LT
56711.04107	z	16.210	0.023	LT
56712.15423	z	16.254	0.033	LT
56713.07523	z	16.228	0.026	LT
56715.02036	z	16.264	0.027	LT
56721.88313	z	16.325	0.029	LT
56723.86738	z	16.326	0.035	LT
56728.01997	z	16.337	0.030	LT
56731.89773	z	16.353	0.032	LT
56733.90845	z	16.379	0.027	LT
56735.92106	z	16.335	0.034	LT
56739.98927	z	16.381	0.029	LT
56741.89896	z	16.428	0.030	LT
56743.98572	z	16.402	0.030	LT
56751.94146	z	16.428	0.031	LT
56753.94364	z	16.431	0.028	LT
56755.04548	z	16.419	0.031	LT
56761.90671	z	16.450	0.058	LT
56762.90040	z	16.439	0.031	LT
56768.92797	z	16.438	0.035	LT
56770.00931	z	16.432	0.030	LT
56770.95330	z	16.445	0.025	LT
56771.97739	z	16.481	0.028	LT
56684.12208	i	16.245	0.022	LT
56685.08659	i	16.237	0.018	LT
56686.07649	i	16.199	0.020	LT
56689.38424	i	16.211	0.036	LCOGT
56692.20445	i	16.219	0.097	LCOGT
56694.00872	i	16.202	0.021	LT
56695.05687	i	16.195	0.022	LT
56696.15155	i	16.189	0.023	LT
56696.17710	i	16.217	0.047	LCOGT
56697.01491	i	16.192	0.026	LT
56698.03063	i	16.200	0.021	LT
56698.97856	i	16.201	0.021	LT
56699.95267	i	16.196	0.024	LT
56700.97002	i	16.203	0.025	LT
56701.93398	i	16.206	0.025	LT
56710.02297	i	16.283	0.021	LT
56711.04013	i	16.275	0.021	LT
56712.15330	i	16.328	0.025	LT
56713.07431	i	16.327	0.021	LT
56715.01944	i	16.352	0.021	LT
56721.88220	i	16.420	0.021	LT
56723.86644	i	16.427	0.023	LT
56728.01904	i	16.487	0.024	LT
56731.89681	i	16.514	0.026	LT
56733.90752	i	16.493	0.025	LT
56735.92014	i	16.508	0.025	LT
56739.98834	i	16.520	0.022	LT
56741.89803	i	16.590	0.022	LT
56743.98480	i	16.570	0.023	LT

Table A1. continued.

MJD	Filter	Magnitude	Magnitude Uncertainty	Telescope
56751.94053	i	16.565	0.025	LT
56753.94272	i	16.577	0.024	LT
56755.04456	i	16.448	0.024	LT
56761.90579	i	16.618	0.026	LT
56762.89948	i	16.597	0.024	LT
56768.92704	i	16.609	0.023	LT
56770.00838	i	16.614	0.026	LT
56770.95238	i	16.608	0.021	LT
56684.12117	r	16.386	0.020	LT
56685.08567	r	16.355	0.021	LT
56686.07558	r	16.340	0.019	LT
56689.38237	r	16.340	0.030	LCOGT
56692.20258	r	16.374	0.045	LCOGT
56694.00780	r	16.369	0.022	LT
56695.05595	r	16.369	0.020	LT
56696.15063	r	16.371	0.020	LT
56696.17523	r	16.362	0.034	LCOGT
56697.01400	r	16.362	0.023	LT
56698.02972	r	16.345	0.021	LT
56698.97764	r	16.401	0.022	LT
56699.95175	r	16.374	0.021	LT
56700.96910	r	16.412	0.027	LT
56701.93306	r	16.429	0.022	LT
56710.02204	r	16.530	0.021	LT
56711.03922	r	16.539	0.020	LT
56712.15239	r	16.579	0.018	LT
56713.07339	r	16.574	0.020	LT
56715.01852	r	16.635	0.020	LT
56721.88128	r	16.708	0.021	LT
56723.86553	r	16.708	0.021	LT
56728.01812	r	16.762	0.024	LT
56731.89589	r	16.821	0.027	LT
56733.90660	r	16.808	0.024	LT
56735.91922	r	16.830	0.022	LT
56739.98740	r	16.865	0.021	LT
56741.89711	r	16.876	0.022	LT
56743.98387	r	16.839	0.022	LT
56751.93961	r	16.879	0.022	LT
56753.94180	r	16.883	0.022	LT
56755.04360	r	16.907	0.023	LT
56761.90486	r	16.886	0.029	LT
56762.89856	r	16.936	0.026	LT
56768.92612	r	16.930	0.020	LT
56770.00746	r	16.947	0.021	LT
56770.95146	r	16.943	0.022	LT
56771.97555	r	16.968	0.020	LT
56682.51157	V	16.300	0.100	ASAS-SN
56684.90883	V	16.420	0.041	*Swift*
56687.03884	V	16.330	0.100	*Swift*
56697.70773	V	16.540	0.081	*Swift*
56702.77099	V	16.390	0.110	*Swift*
56707.92641	V	16.530	0.130	*Swift*
56729.12832	V	17.070	0.170	*Swift*
56734.38386	V	16.730	0.170	*Swift*
56738.53238	V	17.230	0.120	*Swift*
56739.39868	V	17.070	0.110	*Swift*
56744.18546	V	17.180	0.170	*Swift*
56749.78202	V	16.940	0.170	*Swift*
56755.31624	V	17.290	0.180	*Swift*
56760.19089	V	17.160	0.150	*Swift*
56763.39081	V	17.000	0.150	*Swift*
56770.05206	V	17.470	0.260	*Swift*

Table A1. continued.

MJD	Filter	Magnitude	Magnitude Uncertainty	Telescope
56825.86171	*V*	17.620	0.240	*Swift*
56828.44541	*V*	17.080	0.150	*Swift*
56684.12022	*g*	16.533	0.023	LT
56684.33405	*g*	16.528	0.036	LCOGT
56685.08472	*g*	16.516	0.023	LT
56686.07463	*g*	16.509	0.021	LT
56689.38049	*g*	16.503	0.027	LCOGT
56692.20070	*g*	16.595	0.036	LCOGT
56694.00685	*g*	16.590	0.022	LT
56695.05500	*g*	16.594	0.022	LT
56696.14969	*g*	16.575	0.023	LT
56696.17336	*g*	16.559	0.041	LT
56697.01305	*g*	16.597	0.025	LT
56698.02878	*g*	16.617	0.020	LT
56698.97669	*g*	16.602	0.022	LT
56699.95080	*g*	16.633	0.029	LT
56700.96816	*g*	16.638	0.022	LT
56701.93212	*g*	16.636	0.041	LT
56710.02110	*g*	16.837	0.022	LT
56711.03827	*g*	16.844	0.022	LT
56712.15143	*g*	16.885	0.023	LT
56713.07244	*g*	16.897	0.021	LT
56715.01756	*g*	16.944	0.022	LT
56721.88033	*g*	17.077	0.022	LT
56723.86458	*g*	17.104	0.024	LT
56728.01718	*g*	17.157	0.025	LT
56731.89495	*g*	17.187	0.037	LT
56733.90565	*g*	17.233	0.029	LT
56735.91827	*g*	17.266	0.023	LT
56739.98646	*g*	17.296	0.023	LT
56741.89617	*g*	17.353	0.024	LT
56743.98291	*g*	17.348	0.025	LT
56751.93865	*g*	17.378	0.024	LT
56753.94086	*g*	17.379	0.024	LT
56755.04266	*g*	17.402	0.025	LT
56761.90391	*g*	17.347	0.035	LT
56762.89761	*g*	17.436	0.033	LT
56768.92517	*g*	17.452	0.025	LT
56770.00652	*g*	17.445	0.025	LT
56770.95051	*g*	17.442	0.022	LT
56771.97461	*g*	17.468	0.022	LT
56774.95044	*g*	17.466	0.021	LT
56778.95189	*g*	17.470	0.021	LT
56781.91865	*g*	17.481	0.022	LT
56784.92683	*g*	17.487	0.024	LT
56789.92206	*g*	17.498	0.029	LT
56792.93450	*g*	17.495	0.025	LT
56796.90488	*g*	17.522	0.022	LT
56799.89040	*g*	17.500	0.022	LT
56802.96398	*g*	17.525	0.023	LT
56684.89943	*B*	16.690	0.045	*Swift*
56687.03569	*B*	16.720	0.073	*Swift*
56697.70161	*B*	16.830	0.054	*Swift*
56702.76816	*B*	16.800	0.082	*Swift*
56707.84216	*B*	17.170	0.191	*Swift*
56729.12580	*B*	17.480	0.112	*Swift*
56734.38200	*B*	17.710	0.151	*Swift*
56738.52596	*B*	17.740	0.082	*Swift*
56739.39238	*B*	17.740	0.082	*Swift*
56744.18244	*B*	17.650	0.122	*Swift*
56749.78476	*B*	17.720	0.141	*Swift*
56755.31990	*B*	17.510	0.112	*Swift*

Table A1. continued.

MJD	Filter	Magnitude	Magnitude Uncertainty	Telescope
56760.18702	*B*	17.900	0.122	*Swift*
56763.38771	*B*	17.570	0.112	*Swift*
56770.05016	*B*	17.540	0.141	*Swift*
56825.85845	*B*	17.930	0.141	*Swift*
56828.44126	*B*	18.340	0.201	*Swift*
56686.07863	*u*	16.630	0.026	LT
56694.01086	*u*	16.817	0.029	LT
56695.05900	*u*	16.848	0.015	LT
56696.15368	*u*	16.820	0.038	LT
56697.01705	*u*	16.873	0.028	LT
56698.03279	*u*	16.896	0.024	LT
56698.98070	*u*	16.848	0.027	LT
56699.95480	*u*	16.965	0.037	LT
56700.97215	*u*	16.928	0.070	LT
56701.93611	*u*	17.001	0.072	LT
56710.02511	*u*	17.259	0.018	LT
56711.04229	*u*	17.240	0.040	LT
56712.15544	*u*	17.290	0.031	LT
56713.07644	*u*	17.302	0.036	LT
56715.02158	*u*	17.411	0.033	LT
56721.88434	*u*	17.740	0.054	LT
56723.86859	*u*	17.658	0.047	LT
56728.02118	*u*	17.817	0.056	LT
56731.89894	*u*	18.025	0.108	LT
56733.90965	*u*	17.881	0.050	LT
56735.92227	*u*	17.992	0.046	LT
56739.99049	*u*	18.123	0.027	LT
56741.90017	*u*	18.242	0.038	LT
56743.98693	*u*	18.260	0.042	LT
56751.94456	*u*	18.362	0.039	LT
56753.94485	*u*	18.337	0.051	LT
56755.04764	*u*	18.372	0.048	LT
56761.90792	*u*	18.471	0.111	LT
56762.90161	*u*	18.625	0.102	LT
56768.92918	*u*	18.604	0.060	LT
56770.01242	*u*	18.584	0.045	LT
56770.95452	*u*	18.623	0.048	LT
56771.97860	*u*	18.564	0.042	LT
56774.95245	*u*	18.349	0.035	LT
56774.95492	*u*	18.639	0.045	LT
56778.95389	*u*	18.684	0.038	LT
56778.95636	*u*	18.716	0.043	LT
56781.92065	*u*	18.669	0.043	LT
56781.92313	*u*	18.696	0.044	LT
56784.92883	*u*	18.631	0.060	LT
56784.93130	*u*	18.715	0.064	LT
56789.92406	*u*	18.603	0.096	LT
56792.93650	*u*	18.777	0.088	LT
56792.93898	*u*	18.712	0.084	LT
56796.90687	*u*	18.807	0.049	LT
56796.90934	*u*	18.789	0.037	LT
56799.89240	*u*	18.842	0.047	LT
56799.89487	*u*	18.779	0.051	LT
56802.96599	*u*	18.792	0.053	LT
56802.96846	*u*	18.816	0.056	LT
56684.89753	*U*	15.580	0.045	*Swift*
56687.03513	*U*	15.520	0.063	*Swift*
56697.70056	*U*	15.770	0.054	*Swift*
56702.76765	*U*	15.910	0.073	*Swift*
56707.84122	*U*	16.110	0.063	*Swift*
56729.12535	*U*	17.000	0.122	*Swift*
56734.38165	*U*	17.060	0.151	*Swift*

Table A1. continued.

MJD	Filter	Magnitude	Magnitude Uncertainty	Telescope
56738.52485	U	17.000	0.082	*Swift*
56739.39129	U	17.090	0.082	*Swift*
56744.18191	U	17.270	0.132	*Swift*
56749.78160	U	17.420	0.161	*Swift*
56755.31569	U	17.390	0.141	*Swift*
56760.18634	U	17.380	0.122	*Swift*
56763.38716	U	17.510	0.141	*Swift*
56770.04981	U	17.890	0.251	*Swift*
56825.85787	U	18.120	0.211	*Swift*
56828.44054	U	18.230	0.251	*Swift*
56684.89377	$UVW1$	15.110	0.042	*Swift*
56687.03357	$UVW1$	15.090	0.050	*Swift*
56697.69751	$UVW1$	15.550	0.050	*Swift*
56702.76625	$UVW1$	15.710	0.058	*Swift*
56707.83852	$UVW1$	15.910	0.050	*Swift*
56729.07071	$UVW1$	16.870	0.076	*Swift*
56734.38074	$UVW1$	16.920	0.114	*Swift*
56738.52164	$UVW1$	17.090	0.076	*Swift*
56739.38815	$UVW1$	17.120	0.076	*Swift*
56744.18042	$UVW1$	17.220	0.104	*Swift*
56749.78435	$UVW1$	17.360	0.133	*Swift*
56755.31935	$UVW1$	17.400	0.114	*Swift*
56760.18441	$UVW1$	17.830	0.124	*Swift*
56763.38562	$UVW1$	17.820	0.133	*Swift*
56768.73185	$UVW1$	18.180	0.212	*Swift*
56770.04886	$UVW1$	18.000	0.202	*Swift*
56794.79258	$UVW1$	18.550	0.173	*Swift*
56799.45558	$UVW1$	18.150	0.163	*Swift*
56804.11631	$UVW1$	18.390	0.341	*Swift*
56809.31304	$UVW1$	18.500	0.262	*Swift*
56814.44711	$UVW1$	18.220	0.232	*Swift*
56825.85625	$UVW1$	18.600	0.202	*Swift*
56828.43848	$UVW1$	18.530	0.192	*Swift*
56684.91259	$UVM2$	14.770	0.042	*Swift*
56687.03940	$UVM2$	14.780	0.042	*Swift*
56697.70877	$UVM2$	15.430	0.042	*Swift*
56702.77148	$UVM2$	15.640	0.050	*Swift*
56707.92682	$UVM2$	15.850	0.067	*Swift*
56729.12878	$UVM2$	16.880	0.076	*Swift*
56734.38421	$UVM2$	16.910	0.104	*Swift*
56738.53348	$UVM2$	17.140	0.067	*Swift*
56739.39976	$UVM2$	17.000	0.058	*Swift*
56744.18599	$UVM2$	17.130	0.085	*Swift*
56749.78046	$UVM2$	17.330	0.104	*Swift*
56755.31415	$UVM2$	17.600	0.104	*Swift*
56760.19156	$UVM2$	17.740	0.095	*Swift*
56763.39135	$UVM2$	17.690	0.104	*Swift*
56770.05241	$UVM2$	17.710	0.133	*Swift*
56794.59550	$UVM2$	> 18.13	N/A	*Swift*
56799.37997	$UVM2$	18.250	0.182	*Swift*
56804.11453	$UVM2$	18.430	0.222	*Swift*
56809.30874	$UVM2$	18.600	0.153	*Swift*
56814.44225	$UVM2$	18.430	0.133	*Swift*
56825.86227	$UVM2$	18.880	0.182	*Swift*
56828.44612	$UVM2$	18.570	0.133	*Swift*
56684.90137	$UVW2$	15.060	0.042	*Swift*
56687.03627	$UVW2$	15.170	0.050	*Swift*
56697.70267	$UVW2$	15.800	0.042	*Swift*
56702.76867	$UVW2$	15.980	0.058	*Swift*
56707.92452	$UVW2$	16.030	0.058	*Swift*
56729.12627	$UVW2$	16.910	0.085	*Swift*
56734.38236	$UVW2$	17.120	0.104	*Swift*

Table A1. continued.

MJD	Filter	Magnitude	Magnitude Uncertainty	Telescope
56734.38236	$UVW2$	17.120	0.104	*Swift*
56738.52707	$UVW2$	17.130	0.058	*Swift*
56739.39347	$UVW2$	17.170	0.067	*Swift*
56744.18299	$UVW2$	17.230	0.085	*Swift*
56749.78247	$UVW2$	17.270	0.104	*Swift*
56755.31680	$UVW2$	17.460	0.095	*Swift*
56760.18770	$UVW2$	17.690	0.095	*Swift*
56763.38825	$UVW2$	17.690	0.104	*Swift*
56770.05052	$UVW2$	17.580	0.124	*Swift*
56794.59036	$UVW2$	18.470	0.104	*Swift*
56799.37892	$UVW2$	18.150	0.202	*Swift*
56804.11361	$UVW2$	18.490	0.252	*Swift*
56809.30656	$UVW2$	18.230	0.143	*Swift*
56814.43980	$UVW2$	18.770	0.192	*Swift*
56825.85903	$UVW2$	18.930	0.182	*Swift*
56828.44199	$UVW2$	18.650	0.143	*Swift*